Robust Multimode Waveguide Design for Avoided Mode Crossing-Suppressed Microresonators

Ye, Chaochao; Kim, Chanju; Zheng, Yi; Zhou, Yueguang; Kamel, Ayman N.; Zhao, Yanjing; Yvind, Kresten; Pu, Minhao

Published in:
Journal of Lightwave Technology

Link to article, DOI:
10.1109/JLT.2023.3242305

Publication date:
2023

Document Version
Peer reviewed version

Robust Multimode Waveguide Design for Avoided Mode Crossing-Suppressed Microresonators

Chaochao Ye, Chanju Kim, Yi Zheng, Yueguang Zhou, Ayman N. Kamel, Yanjing Zhao, Kresten Yvind, and Minhao Pu

***Abstract* — Microresonator-based optical frequency combs enable many potential applications, from frequency metrology to optical communication. Soliton comb generation relies on dispersion control. For bright soliton generation, it is required to have anomalous group velocity dispersion. However, the avoided mode crossing in the miroresonator can disturb the local dispersion and may prevent the soliton formation. Although the avoided mode crossing may enable dark soliton generation, the unintended avoided mode crossing distorts the comb spectrum. Here, we present a robust multimode waveguide design against intermodal coupling to suppress unintended avoided mode crossing. By engineering the waveguide dimension, the phase mismatch between coupling modes can be increased, which will significantly reduce the modal coupling strength. We experimentally demonstrated the avoided mode crossing-suppressed microresonators in the AlGaAs-on-insulator platform.**

***Index Terms*—Integrated optics devices, nonlinear optics, integrated optics, optical resonators.**

I. INTRODUCTION

Optical frequency combs, consisting of a series of discrete and equally spaced sharp lines in frequency, have revolutionized the precision measurement in the past decades [1]. Traditionally, optical frequency combs are generated using bulky, power-hungry, and expensive table-top mode-locked lasers, which hampers their deployment outside the laboratory. In recent years, microresonator-based Kerr optical frequency combs (microcombs) have emerged and provided an alternative solution to realize comb devices in a more compact, energy-efficient, low-cost, and fully integrated form, which promotes more practical applications. The microcomb is generated by pumping a nonlinear microresonator with an external continuous wave (CW) laser through four-wave mixing (FWM) process [2]–[5]. By carefully balancing the parametric gain and loss as well as dispersion and nonlinearity in the microresonator, a fully coherent state with a broadband and smooth envelope can be achieved, which is called dissipative Kerr soliton (DKS) [6], [7]. The invention of DKS attracts significant attention in the community, unleashing the potential for a much broader application space, such as metrology [8], spectroscopy [9], astronomy [10], microwave photonics [11], and telecommunication [12]. Over the past years, DKS has already been demonstrated in a variety of material platforms (e.g., Si_3N_4 [13], AlN [14], GaP [15], $LiNbO_3$ [16], SiC [17], AlGaAs [18]).

The waveguide dimension of the microresonator is usually engineered to the multimode waveguide to have a low scattering loss, which is critical for optical frequency comb generation [19]–[21]. However, the intermodal coupling may occur in those multimode waveguides and result in avoided mode crossing (AMX) in the microresonators [22], [23]. When two coupled transverse modes approach each other in their resonance, the degeneracy will be lifted, and a hybrid mode with a splitting resonance will appear [24]. The AMX will change the local resonance profile and dispersion [25]. Nevertheless, the Kerr optical frequency comb generation relies on precise group velocity dispersion (GVD) control, which requires anomalous dispersion to provide parametric gain to compensate for the nonlinear phase mismatch [3]. AMX can help to provide local anomalous dispersion to initiate the dark DKS for the microresonators in the normal dispersion regime [26]. Recently, photonic crystal resonators and photonic molecule structures have been used to induce controllable AMX in the normal dispersion regime for frequency comb generation [27], [28]. However, the unexpected occurrence of the AMX induced by intermodal coupling in a single microresonator distorts the comb spectrum and may even prohibit the bright soliton generation [29].

Several methods have been proposed and demonstrated to suppress AMX. A bent waveguide coupler has been introduced to filter out the unwanted polarization mode to address the polarization mode coupling [30]. Similarly, an intracavity taper and curved waveguide coupler were also employed to filter out the undesirable higher-order modes, preventing the higher-order mode interaction [31], [32]. However, the mode filter designs above typically involve structures that may reduce the resonators' quality factor (Q). Another method to suppress the higher-order mode coupling is to reduce the excitation of the higher-order modes. An adiabatic bend has been used to connect the straight and curved sections in the racetrack microresonator to minimize the mode-mismatched transition [23]. However, sharper bends are needed for a small racetrack, which could also change the resonator dispersion and degrade the Q factor.

In this letter, we propose a multimode waveguide design robust against intermodal coupling. The cross-section dimension of the waveguide is engineered to increase the effective index difference between the operational transverse

Manuscript submitted November 27, 2022. This work was supported by the European Research Council (REFOCUS 853522), Innovationsfonden (INCOM 8057-00059B), and the Danish National Research Foundation, SPOC (ref. DNRF123). *(Corresponding author: Minhao Pu.)*

Chaochao Ye, Chanju Kim, Yi Zheng, Yueguang Zhou, Ayman N. Kamel, Yanjing Zhao, Kresten Yvind, and Minhao Pu are with the Department of Photonics Engineering, Technical University of Denmark, Kgs. Lyngby 2800, Denmark. (e-mail: chaye@dtu.dk; ckim@dtu.dk; yizhen@dtu.dk; yuezh@dtu.dk; aynaka@dtu.dk; yanzh@dtu.dk; kryv@fotonik.dtu.dk; mipu@fotonik.dtu.dk).

Color versions of one or more of the figures in this article are available online at http://ieeexplore.ieee.org

mode (TE_{00} mode) and other modes (e.g., TM_{00} and TE_{10} modes). This way, the modal coupling can be significantly suppressed due to the large phase mismatch between the propagating modes. We validate this method in the AlGaAs-on-insulator (AlGaAsOI) based microresonators by comparing the resonator dispersion of different waveguide cross-section dimensions. We identify robust waveguide designs and demonstrate AMX-suppressed microresonators using AlGaAsOI wafers with different thicknesses.

II. Multimode Waveguide Design

Multimode optical waveguides are widely used in integrated nonlinear photonic applications to reduce scattering loss. However, the intermodal coupling may happen in the multimode waveguide. Here, we consider a two-mode system, as shown in Fig. 1. The fields in the microresonator that support two resonator modes can be described by the following coupled equations [25]:

$$\frac{dA_1}{dt} = -\left(\frac{k_{01}}{2} + \frac{k_{c1}}{2} + i\Omega_1\right)A_1 + i\frac{\gamma}{2}A_2 + \sqrt{k_{c1}}S_{in} \quad \ldots (1a)$$

$$\frac{dA_2}{dt} = -\left(\frac{k_{02}}{2} + \frac{k_{c2}}{2} + i\Omega_2\right)A_2 + i\frac{\gamma}{2}A_1 \quad \ldots (1b)$$

Here, S_{in} is the input field. A_1 and A_2 are the intracavity amplitude for the resonator modes 1 and 2, respectively; κ_{01} and κ_{02} are intrinsic loss rates for both modes, κ_{c1} and κ_{c2} are external coupling rates between the resonator and the bus waveguides, Ω_1 and Ω_2 are the frequency detunings, and γ represents the mode coupling rate between the two resonator modes. Generally, there are two methods to suppress the AMX in a single microresonator operating in the resonator mode 1. The first approach is to filter out the coupled (unwanted) resonator mode 2 by increasing its intrinsic loss rate κ_{02} or external coupling rate κ_{c2}. However, the introduced filtering structure may entail increased round-trip loss of the operational resonator mode 1, which is undesirable for attaining a high Q microresonator. Another method is to reduce the mode coupling rate γ. Ideally, the guided transverse modes in the microresonator should be orthogonal – free of the coupling between the two resonator modes (γ=0). Nevertheless, due to the transverse mode hybridization induced by imperfect fabrication or transverse mode-mismatched resonator segments, the intermodal coupling will occur ($\gamma \neq 0$), which induces AMX. As an example, we assumed that transverse modes 1 and 2 have the same intrinsic Q value 1×10^5 and both modes work in the critical condition. Then the transmission spectrum of both modes can be numerically calculated by giving different γ, according to Eq.(1) [33]. The mode coupling rate γ is the ratio between the round-trip mode crosstalk and the round-trip traveling time. And the round-trip mode crosstalk is defined as the maximum normalized converted power of mode 2 (T_2) when mode 1 is injected into the microresonator and can be expressed as $10\log10T_2$ (dB). When the mode coupling is strong (e.g., -10 dB), obvious AMX can be observed in the transmission spectrum, while the AMX can be well suppressed if the mode crosstalk is smaller than -20 dB. Therefore, a small mode coupling strength is critical for suppressing the AMX.

For polarization mode coupling, which may exist in most of the waveguides [34], the transverse mode hybridization may arise from material-inherent birefringence [35], stress-induced birefringence [36], or asymmetrical structure (e.g., tight bending [37], slanted sidewall [38]). The higher the degree of mode hybridization, the stronger the mode coupling strength. Nevertheless, the mode coupling strength depends on the phase-matching condition described in the coupled mode theory [39]. The mode coupling strength can be expressed as $4\kappa^2/(4\kappa^2+\Delta\beta^2)$, where κ represents the field overlap between the modes (degree of mode hybridization), and $\Delta\beta$ is the phase mismatching term (difference of effective mode indices). To suppress the polarization mode coupling, one can increase $\Delta\beta$, which depends on the index difference of the hybridized modes $\Delta n_{(TE00\text{-}TM00)}$.

We numerically investigate the relationship between the mode coupling strength and $\Delta n_{(TE00\text{-}TM00)}$ for 400-nm-high AlGaAsOI waveguides cladded in SiO_2. As an example of asymmetrical structure-induced mode hybridization, we set different slanted sidewall angles (θ=1°,2°, and 5°) for the AlGaAsOI waveguide (see inset of Fig. 2) to induce a varying degree of hybridization through simulation [38]. The TE_{00}-to-TM_{00} mode conversion efficiency was estimated numerically using the eigenmode expansion method (EME, Lumerical MODE Solutions) when the TE_{00} mode was launched into the waveguide. The TE_{00}-to-TM_{00} crosstalk was extracted when the propagation length was swept from 0 μm to 814 μm (the cavity length of the racetrack resonators fabricated for characterization). As shown in Fig. 2, the crosstalk reaches 100% (0 dB) for the waveguide width of 400 nm since it

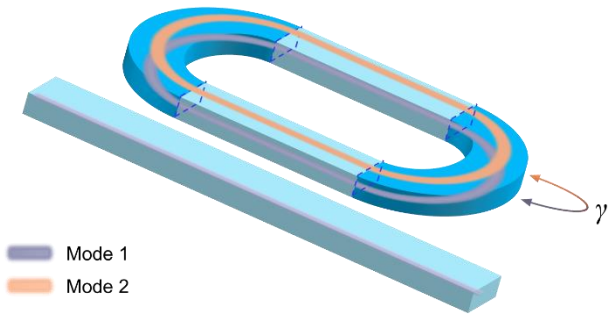

Fig. 1. Schematic of avoided mode crossing in a racetrack microresonator. γ represents the intermodal coupling rate. The blue dashed squares represent the mode-mismatched interface.

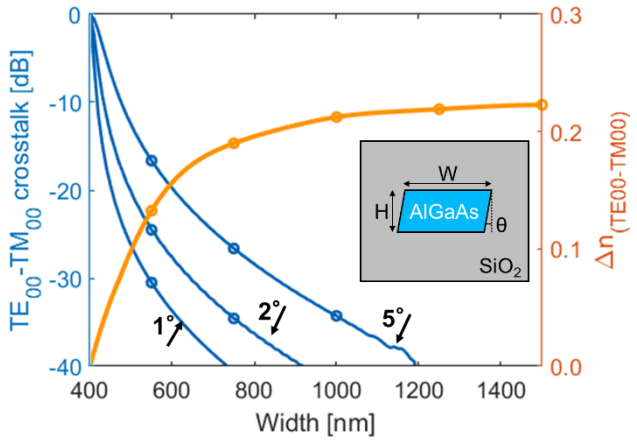

Fig. 2. Simulated TE_{00}-to-TM_{00} crosstalk and index difference $\Delta n_{(TE00\text{-}TM00)}$ versus the waveguide width. Different slanted sidewall angles θ (1°,2°, and 5°) were introduced for different polarization hybridization degrees.

This article has been accepted for publication in IEEE/OSA Journal of Lightwave Technology. This is the author's version which has not been fully edited and content may change prior to final publication. Citation information: DOI 10.1109/JLT.2023.3242305

satisfies the phase matching condition. However, when the waveguide width is increased from 400 nm to 1500 nm, the crosstalk decreases dramatically from 0 dB to below -40 dB as the $\Delta n_{(TE00\text{-}TM00)}$ increases from 0 to 0.22. Therefore, the cross-polarization mode coupling can be well suppressed using a wider waveguide width.

Although the wide waveguide exhibits lower propagation loss, it supports high-order modes, which may induce high-order mode coupling. Apart from fabrication imperfection, the mode-mismatched transition between the straight and curved waveguides for racetrack resonators is another dominant factor that causes spatial mode interaction [23]. The mode field in the multimode waveguide bend is asymmetric with modified effective indices compared with the straight waveguide with the same cross-section. Here, we show that the intermodal crosstalk can be decreased dramatically by increasing the index difference between the fundamental and higher-order modes.

For the higher-order mode coupling, we mainly investigate TE_{00}-TE_{10} mode coupling since the fundamental TE_{00} mode is predominantly coupled to the TE_{10} mode considering in-plane bending [23]. We calculated the TE_{00}-to-TE_{10} mode conversion efficiency after TE_{00} mode propagating through a 400-nm-high straight waveguide, a 180° multimode bend with a radius of 20 μm, and a straight output waveguide, as shown in the insets of Fig. 3. The maximum TE_{00}-TE_{10} mode conversion efficiency within the wavelength range of 1500-1600 nm was simulated using a 3D-FDTD method provided by Lumerical FDTD Solutions. As shown in Fig. 3, the crosstalk was reduced from -11 dB to -34 dB, while the index difference $\Delta n_{(TE00\text{-}TE10)}$ was increased from 0.13 to 0.93 when reducing the waveguide width from 1500 nm to 550 nm. For the waveguide width of 1500 nm, a strong multimode interference was observed in the inset due to the significant crosstalk. A dramatic reduction of intermodal coupling was achieved for the waveguide width of 550 nm. Therefore, the higher-order mode coupling can be well suppressed using a narrower waveguide width. According to the above simulation, both TE_{00}-TM_{00} and TE_{00}-TE_{10} crosstalks can be kept below -20 dB if the waveguide width is kept in the 600-880 nm range. This range can be increased if the cross-polarization mode hybridization and mode-mismatched transition are further reduced.

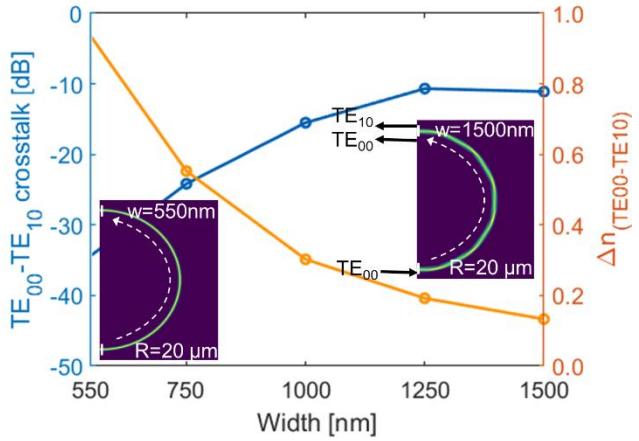

Fig. 3. Simulated TE_{00}-to-TE_{10} crosstalk and index difference $\Delta n_{(TE00\text{-}TE10)}$ versus the waveguide width. The insets show the optical propagation field.

Fig. 4 shows the contour map for index differences $\Delta n_{(TE00\text{-}TE10)}$ (color-shaded contour) and $\Delta n_{(TE00\text{-}TM00)}$ (color-line contour) of different cross-section dimensions for AlGaAsOI waveguides. The black solid line indicates the waveguide dimensions for zero group velocity dispersion (ZGVD). It is seen that the index difference $\Delta n_{(TE00\text{-}TE10)}$ becomes smaller with an increased waveguide width, which infers that the waveguide becomes more susceptible to the TE_{00}-TE_{10} mode coupling with a wider width. Therefore, narrow waveguide widths can be chosen to avoid higher-order mode coupling. However, the index difference between the fundamental TE mode and fundamental TM mode $\Delta n_{(TE00\text{-}TM00)}$ exhibits an opposite trend as it decreases with a decreased waveguide width. A too-narrow waveguide width will then result in polarization coupling. To suppress both TE_{00}-TE_{10} and TE_{00}-TM_{00} mode coupling, one needs to choose a balanced waveguide dimension that provides sufficient index difference value for both $\Delta n_{(TE00\text{-}TE10)}$ and $\Delta n_{(TE00\text{-}TM00)}$. It is worth noting that waveguides with smaller heights have stronger light confinement, which is prone to have a higher degree of mode hybridization [38]. A larger $\Delta n_{(TE00\text{-}TM00)}$ is desired to avoid TE_{00}-TM_{00} mode coupling when the waveguide has a smaller height. Since the reduction of $\Delta n_{(TE00\text{-}TM00)}$ becomes pronounced when the waveguide width is decreased and approaches the ZGVD line, as shown in Fig. 4, we choose a waveguide width (750 nm) close to the ZGVD line as the robust waveguide width for both 300-nm and 400-nm-high microresonators against both polarization coupling and higher-order mode coupling.

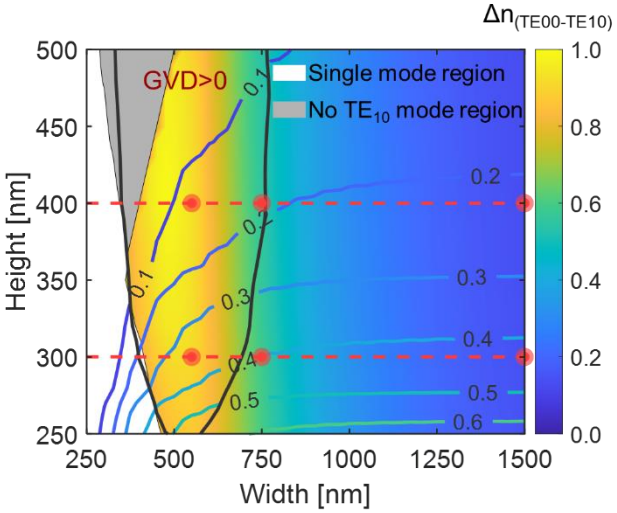

Fig. 4. The calculated index difference $\Delta n_{(TE00\text{-}TM00)}$ (color-line contour) and the $\Delta n_{(TE00\text{-}TE10)}$ (color-shaded contour) for different waveguide dimensions. The black line shows zero dispersion, and the anomalous dispersion is inside. The white area represents a single-mode region, and the grey area shows no TE_{10} mode existence.

III. Fabrication and Characterization

We experimentally demonstrated the AMX suppression in the AlGaAsOI platform [40]. The AlGaAsOI wafer was prepared by wafer-bonding and substrate removal processes [41]. An optimized electron-beam lithography was carried out to define the microresonators' pattern with a negative-tone high-resolution resist, hydrogen silsesquioxane (HSQ) [42]. Then the AlGaAs layer was etched down using an inductively coupled plasma reactive-ion-etching (ICP-RIE) process with

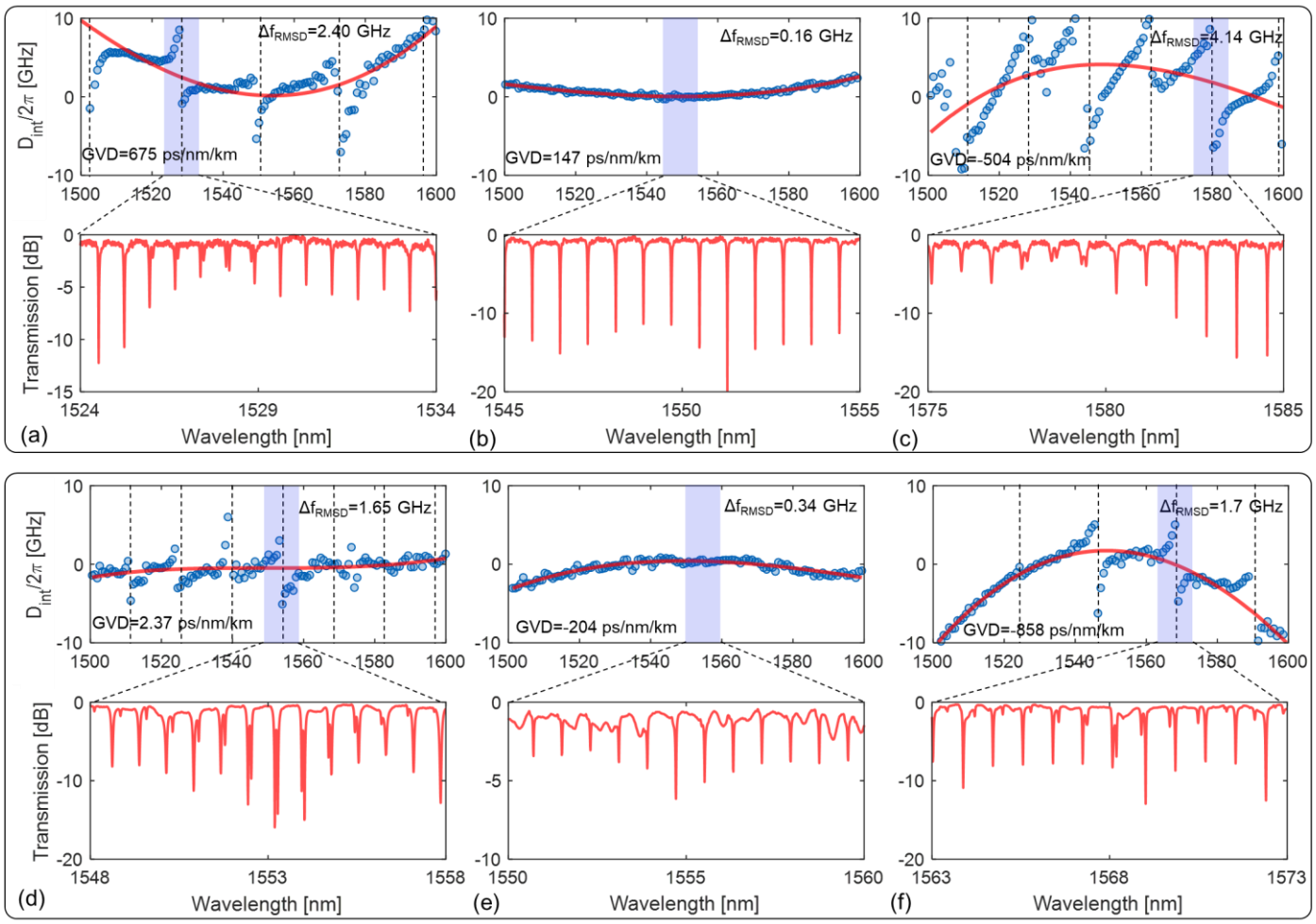

Fig. 5. Measured integrated dispersion and transmission spectrum versus wavelength for different resonator waveguide widths: (a, d) W=550 nm; (b, e) W=750 nm and (c, f) W=1500 nm. The thickness of AlGaAs waveguides is 400nm and 300 nm for (a, b, and c) and (d, e, and f), respectively. The measured GVD and root-mean-squared deviation (Δf_{RMSD}) were shown in the dispersion figures. The dashed lines represent the observed interference period of mode coupling.

chloride-based chemistry. In the end, a 3-μm-thick SiO_2 layer was deposited as the upper cladding using plasma-enhanced chemical vapor deposition (PECVD). In addition, tip-extended inverse tapered edge couplers have also been fabricated in the input and output ports to achieve efficient chip-to-fiber coupling for characterization [33].

Here, to analyze the impact of $\Delta n_{(\mathrm{TE00\text{-}TM00})}$ and $\Delta n_{(\mathrm{TE00\text{-}TE10})}$ on the AMX, 100 GHz racetrack resonators with three different waveguide widths (550, 750, and 1500 nm) have been fabricated. The radius of the curved section was fixed at 20 μm. And the light can be coupled into the resonator by a straight directional coupler, as shown in Fig. 1. Two samples with different nominal waveguide thicknesses (300 and 400 nm) have been fabricated in different batches to verify the generality of the index difference-dependent coupling strength. Dispersion characterization has been performed on both samples.

The dispersion of the microresonators was obtained by a high-resolution transmission spectra measurement assisted by a high-finesse free-space cavity. The transmission spectra are acquired by recording the wavelength scan (continuous-wave external cavity laser) responses of the microresonator devices through an oscilloscope. And the frequency axis was reconstructed by a recorded transmission response of a high-finesse free-space Fabry-Perot cavity with a free-spectral range (FSR) of 100 MHz. More details about the setup can be found in Ref. [43].

The integrated dispersion relative to the center wavelength at μ=0 can be expressed as

$$D_{\mathrm{int}} = w_\mu - w_0 - D_1\mu = \frac{1}{2}D_2\mu^2 + \frac{1}{6}D_3\mu^3 \qquad \ldots (2)$$

where ω_μ is the μth resonance frequency, ω_0 is the center resonance frequency, and D_1, D_2, and D_3 represent the FSR, second-order dispersion, and third-order dispersion parameters, respectively. A positive-valued D_2 implies that the microresonator is in the anomalous GVD regime. The GVD can be obtained from the measured D_2 using the relationship given by GVD=$(2\pi n/\lambda^2)\cdot(D_2/D_1^2)$ [29]. To quantify the AMX perturbation in the integrated dispersion profile, we derive a frequency deviation Δf by subtracting the fitted D_{int} from the measured D_{int} data points.

Fig. 5 shows the measured integrated dispersion and the transmission spectrum of the fabricated microresonators on both samples. As shown in Fig. 5(a) and (d), for the microresonators with a nominal waveguide width of 550 nm, one can find a strong periodic perturbation in the dispersion profile, and clear split resonances can also be observed in the corresponding transmission spectrum, which indicates the

occurrence of AMX. To distinguish the type of AMX, we calculated the interference period at the wavelength of 1550 nm according to the group index difference between two mode families: $\Delta\lambda=\lambda^2/[L\cdot(n_{g,\mathrm{mode1}}-n_{g,\mathrm{mode2}})]$ [23] by using the finite-element method (FEM, Lumerical MODE Solutions). The calculated $\Delta\lambda_{(\mathrm{TE00\text{-}TM00})}$ and $\Delta\lambda_{(\mathrm{TE00\text{-}TE10})}$ are shown in Fig. 6(a). Compared with the observed experimental interference period, we can infer that the AMX was induced by cross-polarization mode coupling for the waveguide width of 550 nm. However, when the waveguide width was increased to 750 nm, the AMX feature was prevented, as shown in Fig. 5(b, e). The larger $\Delta n_{(\mathrm{TE00\text{-}TM00})}$ reduces the cross-polarization modes coupling strength, thus suppressing AMX. Similarly, the $\mathrm{TE_{00}}$-$\mathrm{TE_{10}}$ modes coupling was also suppressed due to the large $\Delta n_{(\mathrm{TE00\text{-}TE10})}$. If the waveguide width increases to 1500 nm, severe frequency deviations appear again due to AMX, as shown in Fig. 5(c, f). From the interference period in Fig. 6(a), one can infer that the AMX is mainly induced by $\mathrm{TE_{00}}$-$\mathrm{TE_{10}}$ coupling. The polarization modes coupling will no longer occur for this large waveguide width due to the large $\Delta n_{(\mathrm{TE00\text{-}TM00})}$, while the modal coupling strength between the $\mathrm{TE_{00}}$ and $\mathrm{TE_{10}}$ modes will increase due to the small index difference $\Delta n_{(\mathrm{TE00\text{-}TE10})}$. We noted that the observed beating frequency is consistent with the simulated overlapping frequency of two transverse modes ($\mathrm{TE_{00}}$-$\mathrm{TM_{00}}$ and $\mathrm{TE_{00}}$-$\mathrm{TE_{10}}$) given by their FSRs.

It is also worth mentioning that the polarization mode coupling occurs for the microresonator with a waveguide cross-section dimension of 300×550 $\mathrm{nm^2}$ (see Fig. 5(d)) even though its cross-polarized index difference $\Delta n_{(\mathrm{TE00\text{-}TM00})}$ is larger than that of the microresonator with a waveguide cross-section dimension of 400×750 $\mathrm{nm^2}$ (a robust design, see Fig. 5(b)). The former waveguide exhibits stronger light confinement than the latter waveguide, which makes it more sensitive to fabrication imperfection (severe mode hybridization). We note that these two samples are fabricated from different batches. The 300-nm thick devices have lower Qs compared with the 400-nm thick devices. For the same waveguide width of 550 nm, the maximum intrinsic Q are 6×10^4 and 1×10^5 for 300- and 400-nm thick resonators, respectively. This may be due to an imperfect fabrication, which may also result in a waveguide sidewall angle and thus a much more severe mode hybridization [33]. Therefore, polarization mode coupling may occur for the 300×550 $\mathrm{nm^2}$ resonator due to a stronger mode hybridization.

Fig. 6(b) shows the root-mean-squared deviation (Δf_{RMSD}) of different waveguide widths for two different thickness samples. Significant dispersion distortion occurred for both small (550 nm) and large waveguide widths (1500 nm). Only the 750-nm-wide waveguides, with their dispersion close to the ZGVD line in Fig. 4, have sufficiently large enough $\Delta n_{(\mathrm{TE00\text{-}TM00})}$ and $\Delta n_{(\mathrm{TE00\text{-}TE10})}$ so that AMX was well suppressed. If a waveguide dimension other than the identified robust design is desired because of the device dispersion requirement, one can employ extra designs to suppress the AMX. For instance, a mode-selective coupler can filter out the unwanted cross-modes ($\mathrm{TM_{00}}$ or $\mathrm{TE_{10}}$) from microresonators to suppress the AMX though the maximum achievable Q may be compromised [30], [32]. Adiabatic or Euler bends can be used to avoid the abrupt transition in racetrack microresonators and thus suppress the AMX [23] [33].

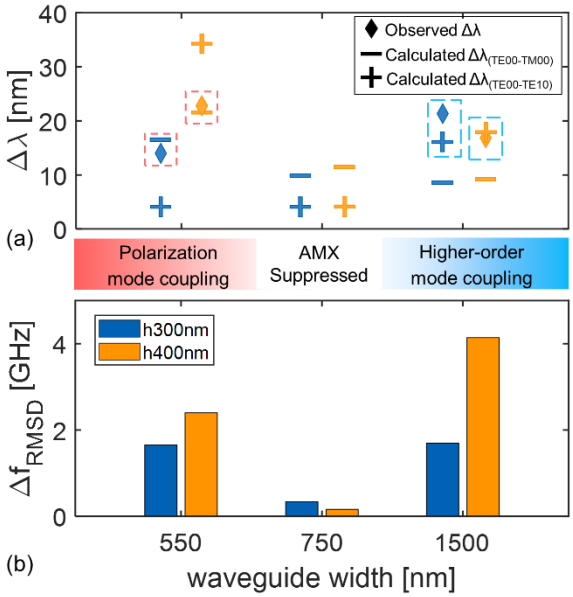

Fig. 6(a). The experimental observed and calculated interference periods Δλ under different waveguide widths. The diamond, bar, and cross shape represent the observed Δλ, calculated $\Delta\lambda_{(\mathrm{TE00\text{-}TM00})}$, and $\Delta\lambda_{(\mathrm{TE00\text{-}TE10})}$, respectively. Blue and orange are for two samples with 300 and 400 nm thicknesses, respectively. (b). Root-mean-squared deviation (Δf_{RMSD}) for different waveguide widths (550, 750, and 1500 nm) with two different thicknesses of 300 nm and 400nm.

IV. conclusion

In conclusion, we have proposed a method to suppress the AMX in the AlGaAsOI microresonators by engineering the waveguide dimension. We have identified robust waveguide dimensions against intermodal coupling and demonstrated AMX-suppressed microresonators in the AlGaAsOI platform. We believe the proposed method also benefits other nonlinear material platforms where soliton comb generation is an important application.

REFERENCES

[1] S. A. Diddams *et al.*, "Optical frequency combs: Coherently uniting the electromagnetic spectrum," *Science (80-.).* **369** (2020).

[2] T. J. Kippenberg *et al.*, "Microresonator-Based Optical Frequency Combs," *Science (80-.).* **332** 555–559 (2011).

[3] A. Pasquazi *et al.*, "Micro-combs: A novel generation of optical sources," *Phys. Rep.* **729** 1–81 (2018).

[4] A. L. Gaeta *et al.*, "Photonic-chip-based frequency combs," *Nat. Photonics* **13** 158–169 (2019).

[5] L. Chang *et al.*, "Integrated optical frequency comb technologies," *Nat. Photonics* **16** 95–108 (2022).

[6] T. Herr *et al.*, "Temporal solitons in optical microresonators," *Nat. Photonics* **8** 145–152 (2014).

[7] T. J. Kippenberg *et al.*, "Dissipative Kerr solitons in optical microresonators," *Science (80-.).* **361** (2018).

[8] Z. L. Newman *et al.*, "Architecture for the photonic integration of an optical atomic clock," *Optica* **6** 680 (2019).

[9] M. Yu *et al.*, "Silicon-chip-based mid-infrared dual-comb spectroscopy," *Nat. Commun.* **9** 6–11 (2018).

[10] E. Obrzud *et al.*, "A microphotonic astrocomb," *Nat. Photonics* **13** 31–35 (2019).

[11] J. Wu *et al.*, "RF Photonics: An Optical Microcombs' Perspective," *IEEE J. Sel. Top. Quantum Electron.* **24** (2018).

[12] A. A. Jørgensen *et al.*, "Petabit-per-second data transmission using a chip-scale microcomb ring resonator source," *Nat. Photonics* **16** (2022).

[13] J. S. Levy *et al.*, "CMOS-compatible multiple-wavelength oscillator for on-chip optical interconnects," *Nat. Photonics* **4** 37–40 (2010).
[14] X. Liu *et al.*, "Aluminum nitride nanophotonics for beyond-octave soliton microcomb generation and self-referencing," *Nat. Commun.* **12** 1–7 (2021).
[15] D. J. Wilson *et al.*, "Integrated gallium phosphide nonlinear photonics," *Nat. Photonics* **14** 57–62 (2020).
[16] Y. He *et al.*, "Self-starting bi-chromatic LiNbO3 soliton microcomb," *Optica* **6** 1138 (2019).
[17] M. A. Guidry *et al.*, "Optical parametric oscillation in silicon carbide nanophotonics," *Optica* **7** 1139 (2020).
[18] G. Moille *et al.*, "Dissipative Kerr Solitons in a III-V Microresonator," *Laser Photonics Rev.* **14** 1–7 (2020).
[19] D. T. Spencer *et al.*, "Integrated waveguide coupled Si3N4 resonators in the ultrahigh-Q regime," *Optica* **1** 153 (2014).
[20] X. Ji *et al.*, "Exploiting Ultralow Loss Multimode Waveguides for Broadband Frequency Combs," *Laser Photonics Rev.* **15** 6–11 (2021).
[21] M. W. Puckett *et al.*, "422 Million intrinsic quality factor planar integrated all-waveguide resonator with sub-MHz linewidth," *Nat. Commun.* **12** 1–8 (2021).
[22] Z. Ye *et al.*, "Integrated, Ultra-Compact High-Q Silicon Nitride Microresonators for Low-Repetition-Rate Soliton Microcombs," *Laser Photonics Rev.* **16** (2022).
[23] X. Ji *et al.*, "Compact, spatial-mode-interaction-free, ultralow-loss, nonlinear photonic integrated circuits," *Commun. Phys.* **5** 84 (2022).
[24] T. J. Kippenberg *et al.*, "Modal coupling in traveling-wave resonators," *Opt. Lett.* **27** 1669 (2002).
[25] Y. Liu *et al.*, "Investigation of mode coupling in normal-dispersion silicon nitride microresonators for Kerr frequency comb generation," *Optica* **1** 137 (2014).
[26] X. Xue *et al.*, "Mode-locked dark pulse Kerr combs in normal-dispersion microresonators," *Nat. Photonics* **9** 594–600 (2015).
[27] Ó. B. Helgason *et al.*, "Dissipative solitons in photonic molecules," *Nat. Photonics* **15** 305–310 (2021).
[28] S. P. Yu *et al.*, "Spontaneous pulse formation in edgeless photonic crystal resonators," *Nat. Photonics* **15** 461–467 (2021).
[29] T. Herr *et al.*, "Mode spectrum and temporal soliton formation in optical microresonators," *Phys. Rev. Lett.* **113** 1–6 (2014).
[30] C. Kim *et al.*, "Suppression of avoided resonance crossing in microresonators," *Opt. Lett.* **46** 3508 (2021).
[31] A. Kordts *et al.*, "Higher order mode suppression in high-Q anomalous dispersion SiN microresonators for temporal dissipative Kerr soliton formation," *Opt. Lett.* **41** 452 (2016).
[32] Y. Zhang *et al.*, "High-order-mode-suppressed multimode microresonators with a low-loss mode remover," *14th Pacific Rim Conf. Lasers Electro-Optics (CLEO PR 2020)* **C11H_2** (2020).
[33] C. Kim *et al.*, "Design and Fabrication of AlGaAs-on-Insulator Microring Resonators for Nonlinear Photonics," *IEEE J. Sel. Top. Quantum Electron.* **29** 1–13 (2022).
[34] S. Ramelow *et al.*, "Strong polarization mode coupling in microresonators," *Opt. Lett.* **39** 5134 (2014).
[35] A. Pan *et al.*, "Fundamental mode hybridization in a thin film lithium niobate ridge waveguide," *Opt. Express* **27** 35659 (2019).
[36] E. Obrzud *et al.*, "Temporal solitons in microresonators driven by optical pulses," *Nat. Photonics* **11** 600–607 (2017).
[37] W. W. Lui *et al.*, "Polarization rotation in semiconductor bending waveguides: a coupled-mode theory formulation," *J. Light. Technol.* **16** 929–936 (1998).
[38] N. Somasiri *et al.*, "Polarization crosstalk in high index contrast planar silica waveguides with slanted sidewalls," *J. Light. Technol.* **21** 54–60 (2003).
[39] H. A. Haus *et al.*, "Coupled-mode theory," *Proc. IEEE* **79** 1505–1518 (1991).
[40] M. Pu *et al.*, "Efficient frequency comb generation in AlGaAs-on-insulator," *Optica* **3** 8–11 (2016).
[41] L. Ottaviano *et al.*, "Low-loss high-confinement waveguides and microring resonators in AlGaAs-on-insulator," *Opt. Lett.* **41** 3996 (2016).
[42] Y. Zheng *et al.*, "High-quality-factor AlGaAs-on-sapphire microring resonators," *J. Light. Technol.* **37** 868–874 (2019).
[43] Y. Zheng *et al.*, "High-quality factor, high-confinement microring resonators in 4H-silicon carbide-on-insulator," *Opt. Express* **27** 13053 (2019).